Materials Advances



View Article Online PAPER



Cite this: Mater. Adv., 2024. **5**, 6309

Received 2nd May 2024, Accepted 25th June 2024

DOI: 10.1039/d4ma00455h

rsc.li/materials-advances

Preparation of bismuth-doped CsPbBr₃ perovskite single crystals for X-ray and gamma-ray sensing applications†

Premkumar Sellan, ** Manigandan Selvan, ** Abida Perveen, ** Din Nasrud, ** Sakthivel Chandrasekar, ^c Pitchaikannu Venkatraman, ^d Devaraj Nataraj, ^b Byung Seong Bae, Damian Chinedu Onwudiwe and Lei Wei*

Perovskite materials are potential photo-absorbers, and their solution-processed perovskite layers are widely reported in photodetection devices. However, defects in perovskites pose a serious challenge to device performance. One possible way to overcome this set-back is growing a perovskite single crystal and deploying it in photon detection devices. Herein, we report the growth of pure and Bi-doped CsPbBr₃ perovskite single-crystals and their high-energy photodetection characteristics. The Bi-doped CsPbBr₃ perovskite single-crystals exhibited good photodetection characteristics in the visible, X-ray and gamma-ray regions. Under an illumination of 470 and 530 nm, the Bi-doped CsPbBr₃ perovskite singlecrystal photodetector displayed a linear response for the biasing voltage ranging from 2 V to 5 V. The device displayed a higher magnitude of photocurrent and exhibited a better ON/OFF ratio of ~596 at λ = 470 nm and ~24 at λ = 530 nm. The gamma ray detection properties of the Bi-doped CsPbBr₃ perovskite single crystal were studied using two different radioactive sources with varying activity levels. A characterization study using a portable X-ray device revealed an excellent response to varying tube voltages and currents. The present study reveals the versatility of the Bi-doped CsPbBr₃ perovskite single-crystals in photon detection under a wide range of illumination.

Introduction

Photodetectors are among the most commonly used sensor devices for acquiring information. Among the various radiation detectors, sensitive gamma-ray detectors are notable in various applications in medical imaging, nuclear energy, scientific research,3 and radiation protection.4,5 In general, two radiation detection techniques are used: direct and indirect. In the direct

210096, P. R. China, E-mail: hw@seu.edu.cn, sivaiiisro@gmail.com

radiation detection technique, high-energy photons are mostly directly converted into electronic signals for which semiconductor crystals can be primary contenders. 4,6,7 Semiconductor crystals are viable as gamma-ray spectral detectors as they have higher stopping power, higher mobility lifetime for efficient charge collection, large resistance to noise for better signal quality, lower trap density for decreased charge trapping, and low cost for a measurable structure.^{8,9} Gamma-ray spectroscopy can resolve the energy of incoming gamma rays and identify radioactive species and isotopes. Germanium has been widely used for gamma-ray spectroscopy for over 40 years. 10,11 Recently, organicinorganic lead halide perovskites have been demonstrated as a promising candidate for developing high performance radiation detectors because of their impressive optical and electronic properties, 8,12 including long change-carrier diffusion lengths, tuneable bandgaps, low defect density,13 high mobility-lifetime (μτ) and unique defect tolerant nature. 14 In recent decades, several semiconducting materials, such as CdTe, 15,16 mercuric iodide (HgI₂),² and CdZnTe (CZT),¹⁷ have been studied for direct radiation detection applications. 18 Unfortunately, none of them is an ideal candidate. Specifically, it is expensive to achieve high-quality spectral grade crystal CdZnTe, which is grown using the hightemperature processing Czochralski method. Lead halide

^a Joint International Research Laboratory of Information Display and Visualization, School of Electronic Science and Engineering, Southeast University, Naniing,

^b Quantum Materials & Devices Laboratory, Department of Physics, Bharathiar University, Coimbatore, Tamil Nadu 641046, India

^c Laboratory of Functional Molecules and Materials, School of Physics and Optoelectronic Engineering, Shandong University of Technology, Zibo, China

^d Radiotherapy & Radiation Medicine, IMS, Banaras Hindu University, Varanasi,

^e Department of Electronics & Display Engineering, Hoseo University, Asan city, Chungnam 31499, Republic of Korea

f Department of Chemistry, School of Mathematics and Physical Sciences, Faculty of Natural and Agricultural Sciences, North-West University Mafikeng Campus, Mmabatho 2735, South Africa

[†] Electronic supplementary information (ESI) available. See DOI: https://doi.org/

Materials Advances Paper

perovskite-based materials are widely used in radiation detection and are considered important in this field.^{6,8} Several studies have tuned the optical and electronic characteristics of halide perovskites by doping them with certain hetero-valent cations. In this respect, cations In³⁺, Ag⁺, Sb³⁺ and Bi³⁺ are particularly interesting because their valence electronic shell is isoelectronic to lead, and the ns² lone pair is essential for defect tolerance. ^{19,20} In a highly symmetric chemical environment, certain ions combine to form narrow-band compounds that are essential for optical applications in halide perovskites. Bi³⁺ is of particular interest as a dopant due to its stability and ionic radius, which is similar to lead (1.03 and 1.19 A).21 One of the critical issues addressed by doping halide perovskites with bismuth is the possibility of shifting the absorption threshold toward longer wavelengths, which was assumed due to the optical bandgap tuning by the doping concentration level. It is found that the doping of bismuth into CsPbX3 ternary compounds, where X (Br or Cl), is known for its high density, high resistivity, and wide bandgap, makes them ideal materials for gamma-ray and X-ray detection at room temperature. The modified solution process was used to grow large single crystals of CsPbX₃ compounds. CsPbBr3 has already been shown to be effective in detecting X-rays.²² However, even a tiny concentration of native defects and impurities can act as traps and recombination centres, negatively impacting the detector's performance. When photoexcited carriers are trapped at defects, it decreases the spectral resolution, and the surface recombination of carriers reduces the charge collection efficiency.^{23,24} Additionally, the value of μτ, an essential property of these materials, is degraded by defect concentrations as low as few ppm or even lower.²⁴ Most measurement techniques lack the sensitivity due to detect defects at low levels.²¹ They cannot ignore native defects, such as vacancies and anti-site defects, which can reduce $\mu\tau$ values and detector efficiency.

In this paper, we successfully doped bismuth into a CsPbBr₃ single crystal and found that it partially replaced Pb²⁺ with Bi³⁺ in the crystal system. Further, we studied their structural and photophysical properties using XRD, SEM, RAMAN and photoluminescence emission spectroscopy. We fabricated a planar-type photodetector device with an Au/Bi-doped CsPbBr₃/Au structure and measured the dark current and photocurrent response at different wavelengths to evaluate the device performance. We also characterized the X-ray and gamma-ray sensing properties of the Bi-doped CsPbBr₃ perovskite single-crystal photodetector and discussed the results in detail.

Experimental methods

Chemicals and reagents

Lead bromide (PbBr₂ \geq 98% Aladdin), cesium bromide (CsBr \geq 99.9% Aladdin), bismuth iodide (BiI₃ \geq 99%, Aladdin) dimethyl sulfoxide (DMSO, \geq 99.9%, Macklin), N,N-dimethylformamide (DMF, ≥99.5%, Aladdin) and cyclohexanol (CyOH) were purchased and used without further purification.

ITC growth of Bi-doped CsPbBr3 single crystals

Single crystals of CsPbBr3 were grown by applying a modified inverse temperature recrystallization process.^{25,26} Initially, a mixture of dimethylsulfoxide (DMSO), dimethylformamide (DMF) and cyclohexanol (CyOH) was prepared. CsBr and PbBr₂ were then dissolved in 40 ml of DMSO at concentrations of 0.5 M and 1 M, respectively. The solution mixture was filtered and heated to a temperature range of 50-85 °C. Once it reached this temperature range, 10 ml of CyOH and DMF (prepared by mixing 5 ml of each) was added to the solution. It was then slowly heated to 80 °C at a rate of about 2 °C per day. At the end of the reaction, a tiny seed crystal was formed inside the beaker. Tiny and transparent seeds were picked and placed on the bottom of the beaker to allow for considerable crystal growth. The temperature of the beaker was initially increased by about 2 °C per day and then maintained at around 82 °C. The beakers were covered with glass slides to avoid the fast evaporation of the DMSO. This slow evaporation process allowed supersaturation to be achieved. After one week, a single bar-shaped crystal was extracted from the solution; then, it was washed and dried in a vacuum. After that, Bi-doped CsPbBr₃ was synthesized, and the top of the BiI₃ layer was coated on the CsPbBr₃ single crystals by the spin coating, followed by annealing at 100 °C for 6 hours. This allows the partial replacement of Pb²⁺ with Bi³⁺ in the crystal system.

Fabrication of a Bi-doped CsPbBr₃ perovskite-based X-ray photodetector

The single-crystal perovskite-based X-ray detector has the vertical structure of Au/Bi-doped CsPbBr₃/Au, and the effective area (electrode area) of the device is 1 cm², which is obtained by the deposition of ~ 30 nm thick gold electrodes on both sides of the sample by thermal evaporation. 27,28

Characterization

The single crystal's surface morphology was analyzed using field emission electron microscopy (FESEM, FEI Quanta 200 FEI). Single crystal elemental analysis using energy dispersive X-ray spectroscopy (EDX) was carried out using an X-act Oxford Instrument system attached to the SEM. The prepared sample's crystallinity and phase purity are measured from X-ray diffraction (XRD) with the Smart Lab 3 diffractometer, covering the 2θ range from 10° to 80°. UV-absorption measurements were carried out by applying a spectrophotometer (Shimadzu UV-2450), and Edinburgh FS5 took photoluminescence (PL) emission studies. The PL lifetime measurements were carried out using a HORIBA Deltaflex IBH time-correlated single-photon counting (TCSPC) system. Perovskite single crystals were characterized by RAMAN measurements using a Horiba LABRAM HR excited by a 785-nm laser. The current-voltage (I-V) and current-time (I-t) features were measured using the Keithley 4200-SCS parameter analyzer tool with an EPS150FA probe station. AUTO LAB Metrohm PGSTAT M101 has a system used for spectral response behaviour under 470 nm and 530 nm wavelength (LED sources Thorlabs).

Characterization of gamma and X-ray sensing applications

The samples of such single crystals of CsPbBr₃ were measured to determine the counts per minute of gamma and X-rays. A data acquisition system was employed, comprising a 60Co **Materials Advances**

radioactive source, 137Cs, and a portable X-ray, connected to a scintillation detector and an analog-digital converter (ADC) electronic system. This system interfaced with a computer and data processing software. The gamma radiation sources (60Co and ¹³⁷Cs) exhibited low activity. The half-life and IL/I0 = 1 ratio determined the maximum expected radioactive energy emitted, indicating no energy absorption by the medium. This value was independent of the radioactive sample's activity. When material was introduced between the radiation detector and the ⁶⁰Co, ¹³⁷Cs, and portable X-ray sources, interactions occurred between the radiation and the matter. In the setup described above, ⁶⁰Co (Energy: 1.25 MeV) with an activity of 1 μCi and ¹³⁷Cs (energy: 0.662 MeV) with an activity of 0.93 µCi were emitted for 60 seconds. The results of the trials demonstrated that the measured disintegrations per second (counts per second) agreed well with the theoretical values with excellent accuracy. Photon counting was performed consistently for 60 seconds, which improved the counting of photon emission events and enabled more precise statistical adjustments. Additionally, measurements were taken at various tube voltages and tube currents using a portable X-ray device (MARS 4.2, Litex).

Results and discussion

Structural characterization of the Bi-doped CsPbBr3 perovskite single crystals

An orange-coloured CsPbBr3 single crystal with a size of 5 mm was grown at 65-85 °C using the inverse temperature recrystallization method (ITC) (represented in Scheme 1). The tiny seed crystals were formed initially, amongst which the transparent seed crystals were selectively chosen to grow large single crystals. On top of the large single crystal (5 mm in size), BiI₃ was spin-coated to achieve the Bi-doped CsPbBr3 perovskite single crystals. During the process, bismuth ions were intercalated into the surface of CsPbBr3 as represented in Fig. S1 (ESI†). The crystallographic characteristics were investigated by XRD characterization. The powder XRD patterns of the synthesised pure CsPbBr3 and Bi3+ intercalated CsPbBr3 perovskite single crystals are shown in Fig. 1. The diffraction peaks found at 15.15°, 27.31°, 30.62°, 46.60°, and 64.56° for both CsPbBr₃ and Bi-doped CsPbBr3 single crystal samples correspond to the

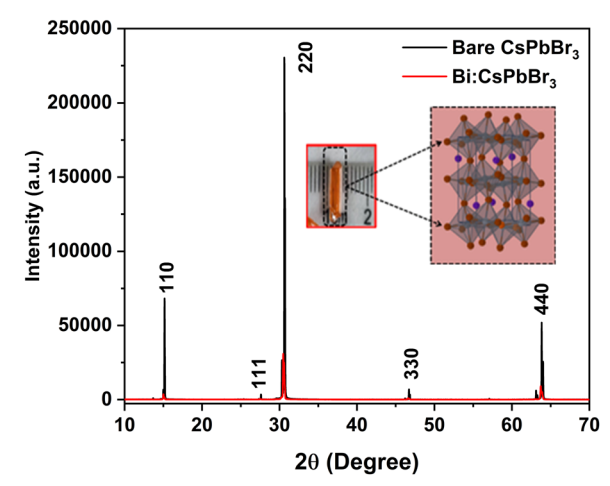


Fig. 1 Room-temperature X-ray diffraction pattern of CsPbBr₃ and Bidoped CsPbBr₃ single crystals. (Inserted image is the single crystal and its crystal structure.).

(110), (111), (220), (330) and (440) planes, which are in good agreement with the reports. 19,29,30 The pure CsPbBr₃ perovskite single crystal exhibits an orthorhombic structure (ICSD 97851) with the *Pnma* space group. A considerable decrease in the diffraction peak intensity is observed for the Bi-doped sample compared to the bare CsPbBr₃ perovskite single crystal. This can be ascribed to the occupation of Bi3+ into the Pb vacancies of the CsPbBr3 perovskite single crystal, as reported elsewhere. ^{29,31} However, the 2θ values were slightly shifted to a lower Braggs angle by 0.10° in the Bidoped CsPbBr₃ single crystal due to the incorporation of bismuth halide, which has different ionic radii that could have reacted interracially or superficially in the pure CsPbBr₃ crystal. Hence, the doping of bismuth resulted in significant changes in the peak intensities of the perovskite diffractogram. 32,33

Photo-physical properties of the Bi-doped CsPbBr₃ perovskite single crystals

Fig. 2 represents the results obtained from the UV-vis absorption and photoluminescence (PL) emission spectroscopic analyses for CsPbBr3 and Bi-doped CsPbBr3 single crystal samples, respectively. It is observed that there are no distinct peaks in the UV-vis absorption spectrum of both samples. Moreover, the



Scheme 1 Schematic representation of CsPbBr₃ single-crystal growth formation.

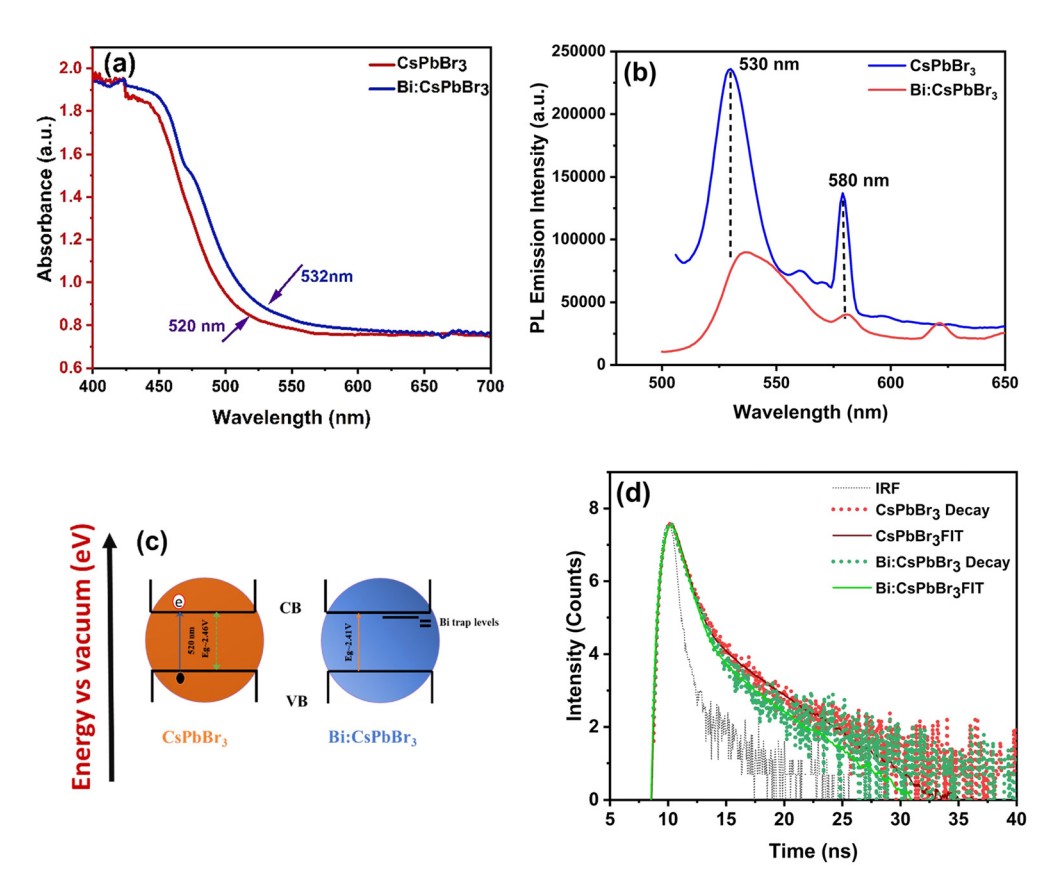


Fig. 2 (a) UV-vis absorbance spectrum, (b) photoluminescence emission spectrum, (c) schematic representation of Bismuth trap state formation near the conduction band edge and (d) TCSPC lifetime decay curve of solution-processed grown CsPbBr₃ single-crystal and Bi-doped CsPbBr₃ samples.

as-prepared CsPbBr3 sample exhibited an absorption onset at 520 nm (Fig. 2a), and the Bi-doped CsPbBr₃ sample displayed a slight red-shift around 532 nm. The Tauc plot for the above samples was drawn, and the calculated direct band gap values were 2.46³⁴⁻³⁶ and 2.41 eV for the pure CsPbBr₃ and Bi-doped CsPbBr₃ single-crystal samples, respectively^{37–39} (Fig. S2, ESI†). The observed redshift in the absorption onset and the corresponding decrease in the band gap value are due to the introduction of shallow traps resulting from the Bi doping process. 38,40 It has to be noted that the difference in the bandgap values of the corresponding samples is not appreciable, which is due to the lower dopant concentration. Similar observations have been reported for the Bi-doping in CsPbX3 single crystals regardless of the halogen element.¹⁹ The photoluminescence emission properties of pure and Bi-doped CsPbBr3 single-crystal samples were studied by recording the PL emission spectrum at an excitation wavelength of 420 nm. As illustrated in Fig. 2b, the pure CsPbBr₃ single crystal exhibited two sharp peaks at 530 and 580 nm, which are attributed to the band edge and Br vacancy centre-based recombination, respectively, as reported elsewhere.36,41 The broadening of the PL emission peak at 530 nm along with a slight red-shift in the case of Bi-doped single crystal is attributed to the introduction of shallow traps during the doping process. This observation is in accordance with the UV-vis absorption analysis of the corresponding

sample. The introduction of trap states is schematically depicted in Fig. 2c.

The PL decay curves of the undoped CsPbBr₃ and Bi-doped CsPbBr₃ single-crystal samples were recorded at their respective emission maxima (at 530 nm) and are shown in Fig. 2d. The average lifetime values are calculated to be 2.67 ns for undoped CsPbBr3, which decreases to 2.25 ns after doping with bismuth. The observed decrease in the PL lifetime values can be attributed to the shallow trap-mediated recombination of photoexcited charge carriers, which is supported by the UV-vis and PL results. Because these shallow traps are introduced inside the band gap near the conduction band edge, a relatively quicker recombination resulted.42 The TCSPC lifetime values of the pure CsPbBr3 and Bi-doped CsPbBr3 single-crystal samples are shown in Table S1 ESI.† The average lifetime value is longer for bare and Bi-doped CsPbBr3 single crystals compared to other nanoparticles and thin films, indicating more efficient extraction of photogenerated electrons. The scanning electron microscopy characterization was carried out, and the micrographs are displayed in Fig. 3a and b. The energy-dispersive X-ray spectroscopy (EDX) elemental graph results of pure CsPBr₃ and Bi-doped CsPbBr₃ single crystal samples indicate the elemental composition and purity of the corresponding samples (Fig. 3c and d). The Raman spectroscopic analysis was carried out for the CsPBr3 and Bi-doped CsPbBr3 single crystal

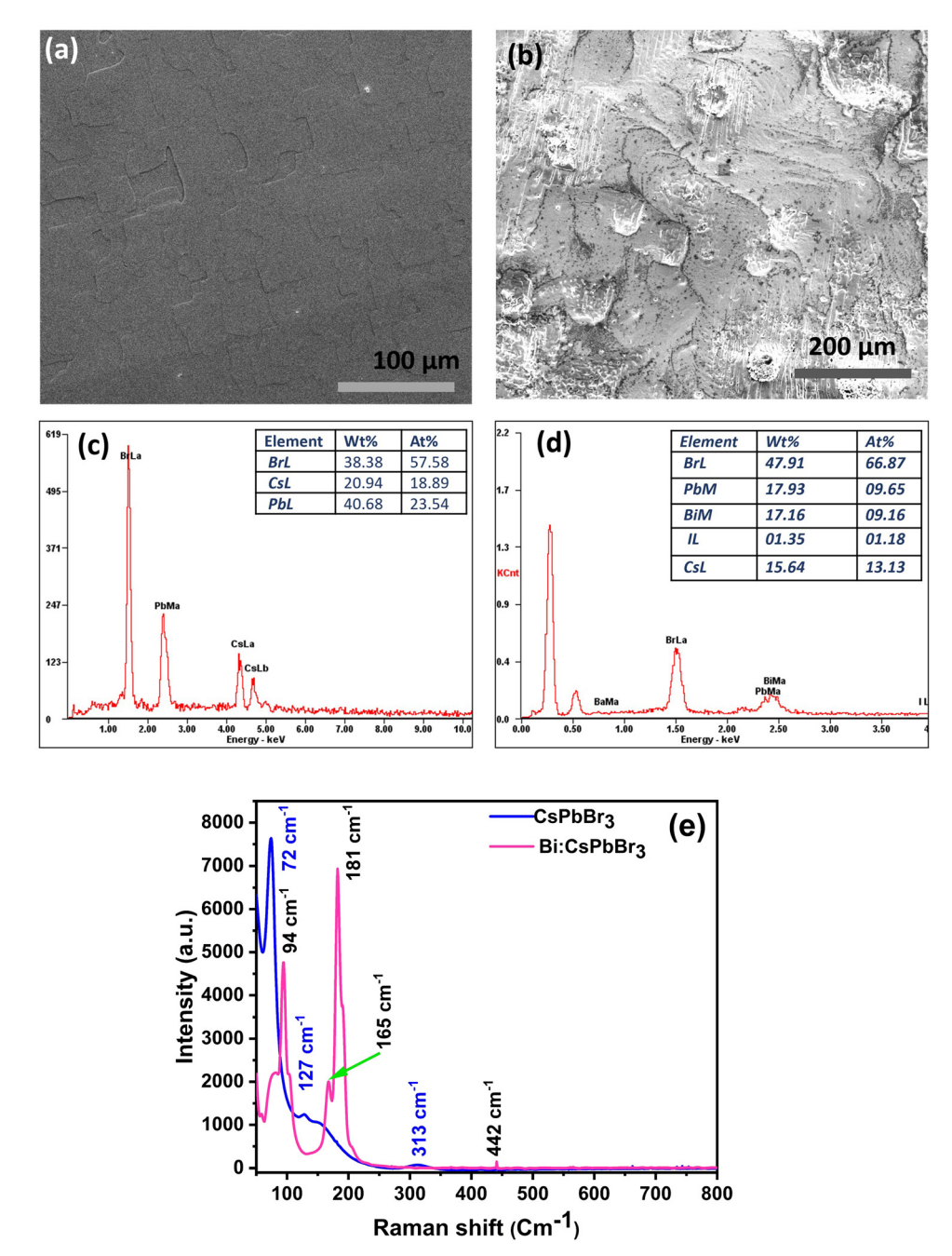


Fig. 3 (a) and (b) Scanning electron microscopy (SEM) image, (c) and (d) energy-dispersive X-ray spectroscopy (EDX) elemental graph and (e) roomtemperature RAMAN spectra (excited at a 785 nm laser) of the CsPbBr3 single crystal and Bi-doped CsPbBr3 samples.

samples, and the results are shown in Fig. 3e. The pure CsPbBr₃ single crystal sample exhibited Raman bands at 72, 127 and 313 cm⁻¹, ³⁶ whereas the Bi-doped sample displayed the bands at 94, 165, 181, and 442 cm^{-1} . The vibrational bands at 72 and 94 cm⁻¹ are assigned to the bending mode of the Br-Pb-Br and its antisymmetric partner, respectively. 43,44 The peak at 165 cm⁻¹ can be assigned to the symmetric Pb-Br stretching mode, whereas the peak at 127 cm⁻¹ is the asymmetric partner. The bands at 165 cm⁻¹ and 313 cm⁻¹ can be attributed to the liberation of cations involving the deformation of the inorganic cage. The observed vibrational modes of the CsPbBr3 and Bidoped single crystals elucidated that they are derived mainly from $[PbBr_6]^{4-}$ anion.

Photocurrent analysis of Bi-doped CsPbBr₃ perovskite single crystals

The orthorhombic CsPbBr3 and Bi-doped single crystals were used to construct the photodetector with Au/(Bi-doped) CsPbBr₃/Au device structure. The band alignment of CsPbBr₃ single crystals with the Au electrode and the schematic diagram of the Bi-doped CsPbBr₃ photodetector are shown in Fig. 4a and b, respectively. Fig. 4c depicts the introduction of shallow trap

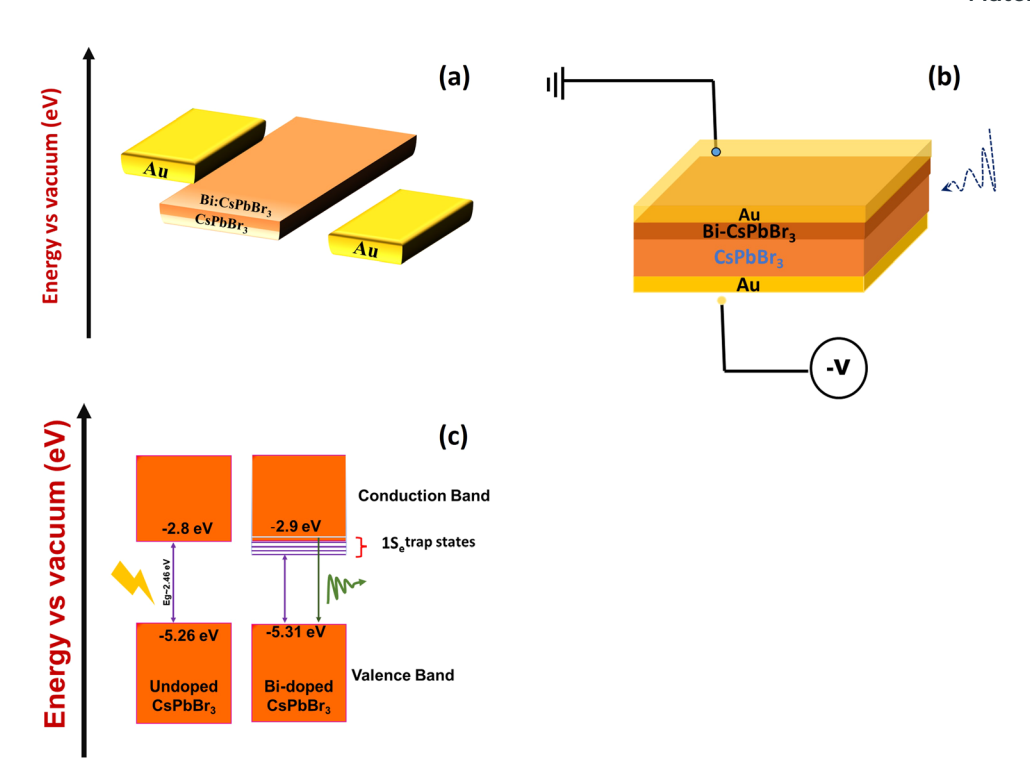


Fig. 4 (a) and (b) Schematic representation of the Bi-doped CsPbBr₃ photocurrent device and (c) Fermi level and defect state density, valence and conduction band edges by incorporating the bismuth dopant. 42,43

states within the band gap of Bi-doped CsPbBr₃, positioned near the bottom of the conduction band edge. The photocurrent measurements were carried out using a low-power illumination of 5 μ W to ensure that the light absorption occurred only on the surface of the single crystal. We measured the current-voltage (I-V) characteristics of the undoped CsPbBr₃ and Bi-doped CsPbBr₃ single-crystal photodetectors in the dark and under light illumination with a bias voltage range of -100 to 100 V. The plots are shown in Fig. 5a and b. The pure CsPbBr₃ single crystal showed a dark current value of 0.026 nA for a biasing voltage of 10 V. Upon illumination, the photocurrent increased to 0.83 nA. The Bi-doped CsPbBr₃ single crystal produced a dark current value of 0.49 nA for a biasing voltage

of 10 V. An interesting increase in the photocurrent value was observed upon illumination. For the same biasing voltage of 10 V, the photocurrent value increased to 5.77 nA. The *I–V* plots exhibited good linearity in the entire measurement range, thereby indicating that the constructed photodetector devices exhibited good responsivity and sensitivity.

In general, perovskite light absorbers suffer from innumerable complications, such as ion migration, lattice distortion and phase segregation, when subjected to an applied electric field. The absence of such instances in the present case indicates the crystal quality of the samples and resultant resistance to phase change under the applied electric field. Thus, the crystal quality can be indirectly evaluated by analyzing the drift in the dark

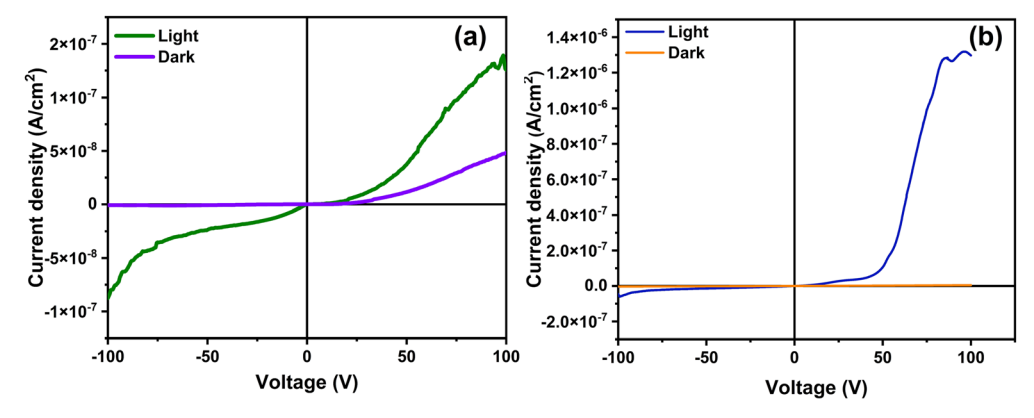


Fig. 5 (I-V) photocurrent studies of (a) the undoped CsPbBr₃ and (b) Bi-doped CsPbBr₃ perovskite single crystal.

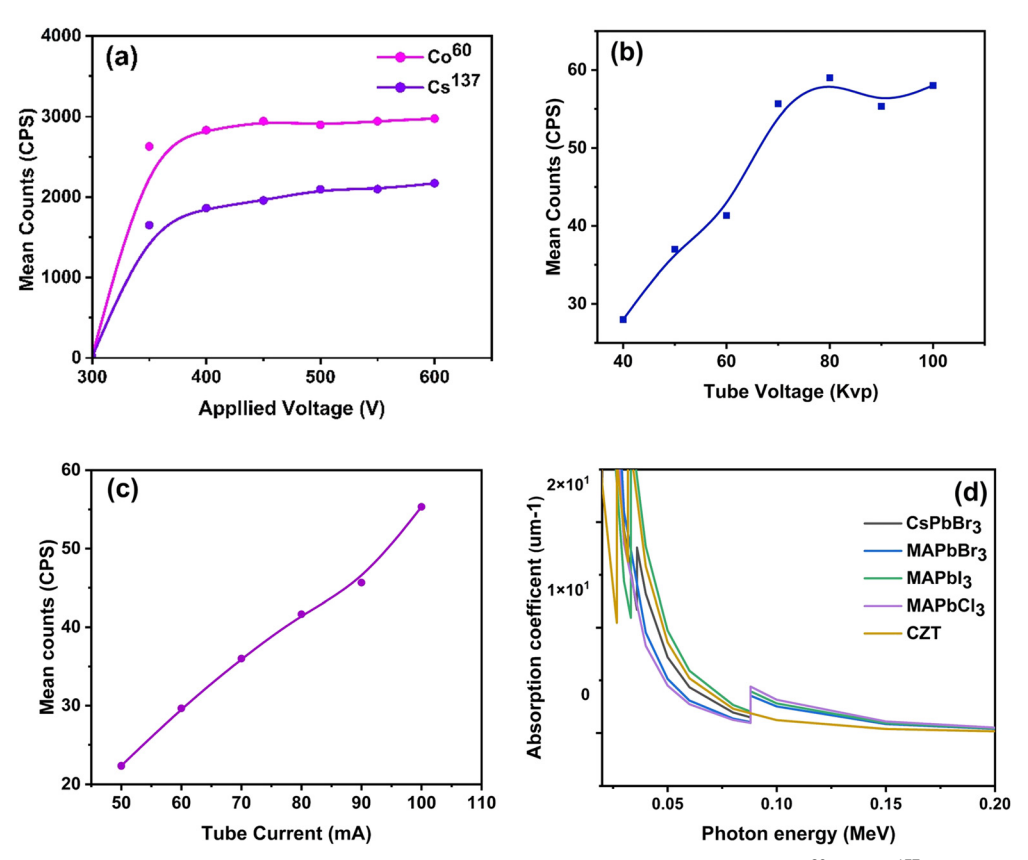


Fig. 6 Schematic representation of gamma and X-ray detection. (a) Optimization of operating voltage using ⁶⁰Co and ¹³⁷Cs. (b) and (c) Characterization at different tube voltages and currents using portable X-ray, and (d) the mass attenuation coefficients of CsPbBr₃, MAPbBr₃, MAPbBr₃ and MAPbCl₃ versus the photon energy according to the XCOM database.⁴⁵

current of the detectors. The detectors were biased using a high electric field of 100 V, and the resulting dark current was recorded, as demonstrated in Fig. 5b.

X-ray and gamma-ray sensing applications

Introducing perovskite materials in gamma-ray detection is particularly challenging due to the high-voltage accelerated ion migration. The as-prepared Bi-doped CsPbBr₃ single crystal was subjected to X-ray and gamma-ray detection. The response characteristics are displayed in Fig. 6a. The Bi-doped CsPbBr₃ single crystal responded well to the Cobalt (60Co, energy - 1.25 MeV, activity = 1 μ Ci) and Cesium (¹³⁷Cs, energy - 0.662 MeV, activity = 0.93 μ Ci) sources within the operating voltage ranging from 300 to 600 V, which falls within the GM region, as shown in Fig. 6a. The ⁶⁰Co produces more particle counts compared to the ¹³⁷Cs; this is because the ⁶⁰Co has higher energy and activity than the ¹³⁷Cs. A portable X-ray characterization study shows a good response to different tube voltages and different tube currents, as shown in Fig. 6b and c. The response of the device was observed as the X-ray tube current varied, which represented the relative dose rate. It was found that the device demonstrated a highly linear response to the variation in the dose rate. This linearity is particularly important for applications in radiation dosimetry. Our recent study showed that the tube voltage ranges from 40 to 100 kV in a unit of 20 kV, and the tube current 122 ranges from 50

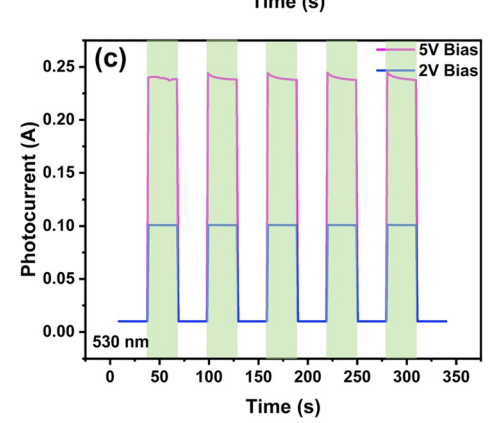
to 300 mA in a unit of 50 mA. Fig. 6d shows the mass attenuation coefficients of CsPbBr3, MAPbBr3, MAPbI3 and MAPbCl3 and CZT versus the photon energy according to the XCOM database. 45 The increase in tube voltage represents the increase in the number of counts (resulting from the increase in the number of particles). It is therefore clear that the Bi-doped CsPbBr₃ single crystal can be used for both X-ray and gamma ray detection and can also be used for high-energy X-ray detection in the future.

Photocurrent analysis of Bi-doped CsPbBr₃ single crystal thin film

We fabricated Bi-doped CsPbBr₃ thin films by dispersing single crystals in DMSO/DMF and spin coating on an FTO substrate. The spin-coated thin films were used to construct photodetectors with FTO/Bi-doped CsPbBr₃/Au device structure. 46,47 Schematic representation of Bi-doped CsPbBr3 perovskite-based thin-film photodetector fabrication is shown in Fig. S3 (ESI†). The crystallographic characteristics were investigated by XRD characterization. The powder XRD patterns of the CsPbBr3 and Bi-doped CsPbBr₃ perovskite thin-film samples on the FTO substrate are shown in Fig. S4 (ESI†). Spectral response curves obtained from the thin-film photodetector study for wavelengths of 470 nm and 530 nm were measured over time at two biasing voltages of 2 V and 5 V. The photocurrent curves in Fig. 7(a-d) show that the prepared thin-film samples exhibit an increase in the photocurrent values as the biasing voltage

Paper

2V Bias OFF (a) (b) 0.25 5V Bias 0.25 0.20 Photocurrent (A) 0.70 0.10 0.10 Photocurrent (A) 30 (s) 0.15 0.05 0.05 ON 0.00 0.00 470 nm 470 nm 100 200 250 0 50 150 300 350 10 20 30 40 50 70 80 Time (s)



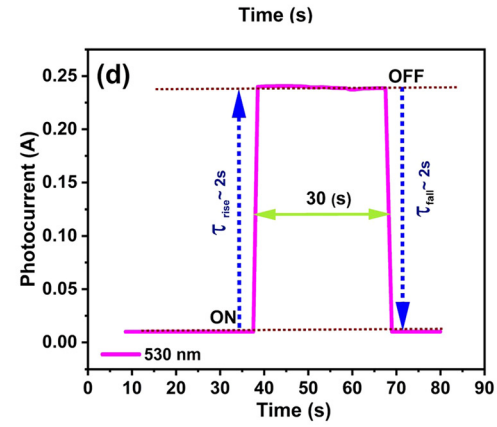


Fig. 7 (I-V) Photocurrent studies of Bi-doped CsPbBr₃ perovskite-based thin-film photodetectors under different light source (a, b) 470 nm and (c, d) 530 nm wavelength at bias 2 V and 5 V.

increases. While irradiating the device with 470 nm and 530 nm light sources, the photocurrent values were observed to be 0.25 mA and 0.20 mA, respectively, for the 5 V bias. The rise and decay time were recorded at an applied bias voltage of 5 V by periodically switching the light ON and OFF at 30-second intervals.

The device exhibited a higher magnitude photocurrent value under a low-intensity power $\lambda=470$ nm LED source with an ON/OFF ratio of $I_{\rm on}/I_{\rm dark}=596$ and for $\lambda=530$ nm LED source, and the ON/OFF ratio was about $I_{\rm on}/I_{\rm dark}\sim24$ at 5 V biasing voltage, recording a fast response and recovery time (Table S2, ESI†). The samples tested with low-power intensity illumination are shown in Fig. S5 (ESI†). The calculated responsivity of the Bi-doped CsPbBr₃ thin-film perovskite photodetector was 0.35 A W⁻¹. Furthermore, based on the current–voltage curves, the Bi-doped CsPbBr₃ thin-film perovskite device demonstrated a better response to blue (470 nm) when compared to the green (530 nm) wavelength. The device maintained good performance after being stored under ambient conditions for over three months.

Conclusions

We successfully demonstrated the synthesis of high-quality Bidoped CsPbBr₃ single crystals by using the ITC solution growth method, and their photophysical properties and sensing were investigated in detail. The photophysical characterization of the CsPbBr₃ and Bi-doped CsPbBr₃ system and enhancement in the photocurrent measurements were tested with different radioactive sources, and we characterized both X-ray and gamma rays at various activity levels. A portable X-ray characterization study demonstrated an excellent response to different tube voltages and tube currents. This linearity is particularly important for applications in radiation dosimetry. The thin-film-based photodetector results reflected the device performance of the Bi-doped CsPbBr₃ thin-film perovskite device, which demonstrated a better response to blue (470 nm) when compared to green (530 nm) wavelength, even after being stored under ambient conditions over three months. Based on the overall performance, the Bi-doped CsPbBr₃ perovskite crystal can be used for X-rays and gamma rays. High-energy X-rays can also be detected in the near future using this crystal.

Author contributions

Premkumar Sellan. and Lei Wei conceived the idea. Premkumar Sellan prepared the samples and performed the optical and morphological characterization, and collected the data. Premkumar Sellan conceived the idea for the construction of a photocurrent device. Abida Perveen, Din Nasrud writing review & editing and supporting for samples testing. Manigandan Selvam data curation, Sakthivel Chandrasekar review & editing. Pitchaikannu Venkatraman supporting the characterization of radiation detection, Byung Seong Bae and Damian Chinedu

Onwudiwe writing review & editing. Premkumar Sellan and Lei Wei analyzed the collected data and wrote the manuscript and all other authors took part in their respective data analyses.

Data availability

All the related experimental data that support the findings of this research work are accessible from the corresponding author by means of a reasonable request. Some of the experimental results, such as Fig. S1–S5, are provided in the ESI† data file.

Conflicts of interest

There are no conflicts to declare.

Acknowledgements

This work is financially supported by International cooperative research project of Jiangsu province (BZ2022008), National Key Research and Development Program of China (2022YFE0139100), National Natural Science Foundation Project of China (62175028), Program 111_2.0 in China (BP0719013).

Notes and references

- 1 F. Liu, *et al.*, Recent Progress in Halide Perovskite Radiation Detectors for Gamma-Ray Spectroscopy, *ACS Energy Lett.*, 2022, 7, 1066–1085.
- 2 J. S. Iwanczyk, W. F. Schnepple and M. J. Masterson, The effect of charge trapping on the spectrometric performance of HgI2 gamma-ray detectors, *Nucl. Instrum. Methods Phys. Res., Sect. A*, 1992, 322, 421–426.
- 3 H. L. Malm, T. W. Raudorf, M. Martini and K. R. Zanio, Gamma Ray Efficiency Comparisons for Si(Li), Ge, CdTe and HgI2 Detectors, *IEEE Trans. Nucl. Sci.*, 1973, **20**, 500–509.
- 4 M. Partridge, B.-M. Hesse and L. Müller, A performance comparison of direct- and indirect-detection flat-panel imagers, *Nucl. Instrum. Methods Phys. Res., Sect. A*, 2002, **484**, 351–363.
- 5 D. V. Kalaga, *et al.*, Some industrial applications of gammaray tomography, *J. Taiwan Inst. Chem. Eng.*, 2009, **40**, 602–612.
- 6 L. Protesescu, *et al.*, Nanocrystals of Cesium Lead Halide Perovskites (CsPbX ₃, X = Cl, Br, and I): Novel Optoelectronic Materials Showing Bright Emission with Wide Color Gamut, *Nano Lett.*, 2015, **15**, 3692–3696.
- 7 X. Geng, *et al.*, Lead-Free Halide Perovskites for Direct X-Ray Detectors, *Adv. Sci.*, 2023, **10**, 2300256.
- 8 H. Wei and J. Huang, Halide lead perovskites for ionizing radiation detection, *Nat. Commun.*, 2019, **10**, 1066.
- 9 L. Zhao, et al., High-yield growth of FACsPbBr3 single crystals with low defect density from mixed solvents for gamma-ray spectroscopy, Nat. Photonics, 2023, 17, 315–323.
- 10 R. J. Cooper, M. Amman and K. Vetter, High resolution gamma-ray spectroscopy at high count rates with a

- prototype High Purity Germanium detector, *Nucl. Instrum. Methods Phys. Res.*, *Sect. A*, 2018, **886**, 1–6.
- 11 A. J. Tavendale, Large Germanium Lithium-Drift p-i-n Diodes for Gamma-Ray Spectroscopy, *IEEE Trans. Nucl. Sci.*, 1965, 12, 255–264.
- 12 R. Gupta, *et al.*, Synthesis and characterization of allinorganic (CsPbBr3) perovskite single crystals, *Mater. Adv.*, 2022, 3, 7865–7871.
- 13 Y. Feng, *et al.*, Low defects density CsPbBr3 single crystals grown by an additive assisted method for gamma-ray detection, *J. Mater. Chem. C*, 2020, **8**, 11360–11368.
- 14 J. Kang and L. W. Wang, High Defect Tolerance in Lead Halide Perovskite CsPbBr3, *J. Phys. Chem. Lett.*, 2017, 8, 489–493.
- 15 Y. Eisen, A. Shor and I. Mardor, CdTe and CdZnTe gamma ray detectors for medical and industrial imaging systems, *Nucl. Instrum. Methods Phys. Res., Sect. A*, 1999, **428**, 158–170.
- 16 Y. Eisen, A. Shor and I. Mardor, CdTe and CdZnTe X-ray and gamma-ray detectors for imaging systems, *IEEE Trans. Nucl.* Sci., 2004, 51, 1191–1198.
- 17 K. Lee *et al.*, *Development of x-ray and gamma-ray CZT detectors for homeland security applications*, ed. R. S. Harmon, J. H. Holloway Jr. & J. T. Broach, 2010, 766423, DOI: 10.1117/12.850113.
- 18 C. Szeles, CdZnTe and CdTe materials for X-ray and gamma ray radiation detector applications, *Phys. Status Solidi B*, 2004, 241, 783–790.
- 19 E. Jedlicka, *et al.*, Bismuth Doping Alters Structural Phase Transitions in Methylammonium Lead Tribromide Single Crystals, *J. Phys. Chem. Lett.*, 2021, 12, 2749–2755.
- 20 P. K. Nayak, *et al.*, Impact of Bi ³⁺ Heterovalent Doping in Organic-Inorganic Metal Halide Perovskite Crystals, *J. Am. Chem. Soc.*, 2018, **140**, 574–577.
- 21 O. A. Lozhkina, *et al.*, Invalidity of Band-Gap Engineering Concept for Bi³⁺ Heterovalent Doping in CsPbBr₃ Halide Perovskite, *J. Phys. Chem. Lett.*, 2018, **9**, 5408–5411.
- 22 J. Peng, et al., Crystallization of CsPbBr₃ single crystals in water for X-ray detection, Nat. Commun., 2021, 12, 1531.
- 23 J. Ma, T. J. Miao and J. Tang, Charge carrier dynamics and reaction intermediates in heterogeneous photocatalysis by time-resolved spectroscopies, *Chem. Soc. Rev.*, 2022, 51, 5777–5794.
- 24 M. Sebastian, *et al.*, Excitonic emissions and above-band-gap luminescence in the single-crystal perovskite semiconductors CsPbBr₃ and CsPbCl₃, *Phys. Rev. B: Condens. Matter Mater. Phys.*, 2015, **92**, 235210.
- 25 M. I. Saidaminov, et al., High-quality bulk hybrid perovskite single crystals within minutes by inverse temperature crystallization, Nat. Commun., 2015, 6, 7586.
- 26 Y. Rakita, *et al.*, Low-Temperature Solution-Grown CsPbBr₃ Single Crystals and Their Characterization, *Cryst. Growth Des.*, 2016, **16**, 5717–5725.
- 27 S. Premkumar, D. Nataraj, G. Bharathi, S. Ramya and T. D. Thangadurai, Highly Responsive Ultraviolet Sensor

Paper

Based on ZnS Quantum Dot Solid with Enhanced Photo-

28 S. Premkumar, D. Nataraj, G. Bharathi, O. Y. Khyzhun and T. D. Thangadurai, Interfacial Chemistry-Modified QD-Coupled CdTe Solid Nanowire and Its Hybrid with Graphene Quantum Dots for Enhanced Photocurrent Properties, *ChemistrySelect*, 2017, 2, 10771–10781.

current, Sci. Rep., 2019, 9, 18704.

- 29 Y. Wang, *et al.*, Epitaxial Growth of Large-Scale Orthorhombic CsPbBr₃ Perovskite Thin Films with Anisotropic Photoresponse Property, *Adv. Funct. Mater.*, 2019, **29**, 1904913.
- 30 M. Li, X. Zhang, K. Matras-Postolek, H.-S. Chen and P. Yang, An anion-driven Sn²⁺ exchange reaction in CsPbBr ₃ nanocrystals towards tunable and high photoluminescence, *J. Mater. Chem. C*, 2018, **6**, 5506–5513.
- 31 Ch. K. Møller, Crystal Structure and Photoconductivity of Caesium Plumbohalides, *Nature*, 1958, **182**(4647), 1436.
- 32 R. Gupta, *et al.*, Synthesis and characterization of allinorganic (CsPbBr₃) perovskite single crystals, *Mater. Adv.*, 2022, 3, 7865–7871.
- 33 J. Zhang, *et al.*, n-Type Doping and Energy States Tuning in CH₃NH₃Pb_{1-x}Sb_{2x/3}I₃ Perovskite Solar Cells, *ACS Energy Lett.*, 2016, **1**, 535–541.
- 34 H. Lan, *et al.*, All-inorganic CsPbBr₃ thin-film solar cells prepared by single-source physical vapor deposition, *Mater. Sci. Semicond. Process.*, 2021, **132**, 105869.
- 35 Y. He, *et al.*, High spectral resolution of gamma-rays at room temperature by perovskite CsPbBr₃ single crystals, *Nat. Commun.*, 2018, **9**, 1609.
- 36 X. Wei, *et al.*, Low-temperature architecture of a cubic-phase CsPbBr₃ single crystal for ultrasensitive weak-light photodetectors, *Chem. Commun.*, 2021, 57, 7798–7801.
- 37 R. Gupta, *et al.*, Synthesis and characterization of allinorganic (CsPbBr₃) perovskite single crystals, *Mater. Adv.*, 2022, 3, 7865–7871.

- 38 O. A. Lozhkina, *et al.*, Invalidity of Band-Gap Engineering Concept for Bi³⁺ Heterovalent Doping in CsPbBr₃ Halide Perovskite, *J. Phys. Chem. Lett.*, 2018, **9**, 5408–5411.
- 39 R. Wang, *et al.*, Bi³⁺-doped CH₃NH₃PbI₃: Red-shifting absorption edge and longer charge carrier lifetime, *I. Alloys Compd.*, 2017, **695**, 555–560.
- 40 X. Zhang, et al., All-Inorganic Perovskite Nanocrystals for High-Efficiency Light Emitting Diodes: Dual-Phase CsPbBr₃-CsPb₂Br₅ Composites, Adv. Funct. Mater., 2016, 26, 4595–4600.
- 41 M. Chen, Y. Yuan, Y. Liu, D. Cao and C. Xu, High-quality all-inorganic CsPbBr₃ single crystals prepared by a facile one-step solution growth method, RSC Adv., 2022, 12, 14838–14843.
- 42 V. Naresh, T. Jang, Y. Pang and N. Lee, Highly luminescent dual-phase CsPbBr₃/Cs₄PbBr₆ microcrystals for a wide color gamut for backlight displays, *Nanoscale*, 2022, **14**, 17789–17801.
- 43 S. Ghosh, *et al.*, Vibrational study of lead bromide perovskite materials with variable cations based on Raman spectroscopy and density functional theory, *J. Raman Spectrosc.*, 2021, 52, 2338–2347.
- 44 O. Yaffe *et al.*, in The nature of dynamic disorder in lead halide perovskite crystals (Conference Presentation), ed. Bakulin, A. A., Banerji, N. & Lovrincic, R., *Physical Chemistry of Interfaces and Nanomaterials XV 48*, SPIE, 2016, DOI: 10.1117/12.2236330.
- 45 M. J. Berger et al., XCOM: Photon Cross Sections Database: NIST Standard Reference Database 8, NIST, 2013, 2013.
- 46 S. Premkumar, et al., Stable Lead-Free Silver Bismuth Iodide Perovskite Quantum Dots for UV Photodetection, ACS Appl. Nano Mater., 2020, 3, 9141–9150.
- 47 S. Premkumar, et al., Ag₂BiI₅ Perovskite Quantum Dots Passivated with Oleylamine Sulfide for Solar Cells and Detection of Cu(II) Ions, ACS Appl. Nano Mater., 2021, 4, 9895–9903.